inorganics

MDPI

Article

Synthesis of MgO Doped with $CoO/MgAl_2O_4$, $NiO/MgAl_2O_4$, and $CuO/MgAl_2O_4$ in a Single Pot for Efficient Dye Adsorption

Salah H. Elhory [1], Tarig G. Ibrahim [2], Mohamed R. Elamin [3], Faisal K. Algethami [3], Mohamed S. Eltoum [1], Babiker Y. Abdulkhair [3,*] and Mutaz Salih [3]

[1] Chemistry Department, Faculty of Science, Sudan University of Science and Technology (SUST), Khartoum P.O. Box 13311, Sudan
[2] Basic Science Research Center, Deanship of Scientific Research, Imam Mohammad Ibn Saud Islamic University (IMSIU), P.O. Box 90950, Riyadh 11623, Saudi Arabia; tariggaffer@gmail.com
[3] Chemistry Department, College of Science, Imam Mohammad Ibn Saud Islamic University (IMSIU), P.O. Box 90950, Riyadh 11623, Saudi Arabia; mrabuzaid@imamu.edu.sa (M.R.E.); fkalgethami@imamu.edu.sa (F.K.A.); meamin@imamu.edu.sa (M.S.)
* Correspondence: byabdulkhair@imamu.edu.sa

Abstract

A simple method employing dextrose as a capping agent was adopted for making $MgAl_2O_4$@MgO (AM), 5%NiO-$MgAl_2O_4$@MgO (AMNi), 5%CoO-$MgAl_2O_4$@MgO (AMCo), and 5%CuO-$MgAl_2O_4$@MgO (AMCu) nanocomposites. The average particle sizes, determined via SEM, were in the range of 21.6–51.4 nm, 9.8–13.8 nm, 19.1–32.2 nm, and 9.2–31.2 nm for AM, AMCu, AMNi, and AMCo, respectively. The nanosorbents exhibited type IV isotherm curves and type H3 hysteresis loops, signifying mesoporous properties. The AM, AMCu, AMNi, and AMCo exhibited surface areas of 69.47, 95.87, 86.23, and 75.87 m^2/g, respectively. The pseudo second order described the indigo carmine (IDC) sorptions onto AM, AMCu, AMNi, and AMCo. The liquid film diffusion regulated IDC sorption on AMNi and AMCo, whereas the intraparticle diffusion was the dominant model on AM and AMCu. The AMCu's showed a q_t value of 127 mg g^{-1} from a 50 mg L^{-1} IDC solution at 20 °C, and 286.2 mg g^{-1} from a 200 mg L^{-1} IDC solution at 50 °C, establishing its capability for treating contaminated water. The IDC sorption onto AMCu aligns with the Freundlich model, which may elucidate the elevated q_t value of AMCu. Elevating the temperature induced the IDC sorption on AMCu, indicating its endothermic nature, and the negative ΔG° implied that the IDC sorption by AMCu was spontaneous. A 5.0 and 10.0 mg L^{-1} IDC concentration in natural water samples was treated by the AMCu, which showed 100.0% efficacy for both groundwater samples; however, its efficacy toward the 5 and 10 mg L^{-1} IDC in seawater was 99.23% and 89.78%, respectively. The MACu's efficiency throughout four reuse cycles decreased by only 7.21%, demonstrating excellent stability and reusability performance.

Keywords: magnesium aluminate; indigo carmine; adsorption; transition metals

Check for updates

Academic Editor: Antonino Gulino

Received: 28 November 2025
Revised: 27 January 2026
Accepted: 28 January 2026
Published: 30 January 2026
Corrected: 30 March 2026

Copyright: © 2026 by the authors. Licensee MDPI, Basel, Switzerland. This article is an open access article distributed under the terms and conditions of the Creative Commons Attribution (CC BY) license.

1. Introduction

The severity of water pollution stands as one of the primary threats to life arising from the global economic development that humanity has adopted [1,2]. The extensive production and application of dyes on a worldwide scale result in wastewater that poses significant environmental risks. Various industries currently discharge effluents containing organic contaminants into aquatic ecosystems. The industries participating in this dilemma encompass manufacturing, textiles, paper, leather, plastic, ink, and cosmetics. Industries of

this nature consume significant quantities of water and generate a wide array of pollutants, including dyes, additives, suspended solids, heavy metals, and solvents. Consequently, these contaminants reach water supplies, posing a significant threat to aquatic ecosystems and the whole environment [3,4]. Every living organism is impacted by the harmful effects of these pollutants, even when present in very low concentrations [5–8]. Dyes are frequently identified as the primary contaminants in many industrial wastewater [9]. Indigo Carmine (IDC) dye is extensively employed across various industries due to its vibrant color [8]. This substance is classified as a toxic dye due to its harmful effects on human health when it comes into contact with the skin and eyes. The IDC structure consists of four benzene rings along with two negatively charged sulfonate groups, which contribute to its non-biodegradable nature, high toxicity, and carcinogenic effects on both humans and aquatic life. The consumption of this dye in elevated concentrations appeared to be fatal due to its carcinogenic properties and potential to cause reproductive, developmental, neurological, and acute toxic effects. This substance is recognized for its potential to induce a range of hypertension, from mild to severe, as well as various cardiovascular and respiratory impacts. IDC has the potential to inflict irreversible harm on the cornea and conjunctiva, aligning with the World Health Organization's established limit concentration of 0.005 mg L^{-1} for IDC [7–11]. Consequently, it is crucial to eliminate IDC from wastewater and industrial discharge sources. A variety of unconventional nano-sorbents, such as carbonaceous materials, metal oxides, and nanocomposites, have been explored for the elimination of IDC [2,12,13]. The technique of photocatalytic degradation for IDC in wastewater has been utilized in various studies, indicating its potential for removing such pollutants through this method [14]. Adsorption is an energy-conserving technique that is simple, straightforward, highly effective, and an easily executed process, which does not release toxic substances [15]. The π/π bonding and Van der Waals force are characteristic of physisorption, whereas chemisorption occurs when bonding between pollutants and sorbents is formed. Metal oxide nanomaterials have been studied for their potential to combat water pollutants, including dyes, pharmaceuticals, and heavy metals. Due to its low specific gravity, MgO exhibits high strength and stiffness, making it suitable for numerous potential applications. These include, but are not limited to, biosensors, computers, electronics, vehicles, aircraft, adsorbents, catalysts, superconducting products, and batteries [16]. Both aluminum and magnesium are targets for various applications due to their widespread mineral abundance on Earth and their relative safety and ease of refinement [17].

There are several methods for preparing oxides of alumina and magnesia, which have been utilized as catalysts, catalyst supports, adsorbents, and wear-resistant coatings, and do not require a specific preparation method. Al_2O_3-MgO exhibits a higher surface area and adsorption capacity than Al_2O_3 and/or MgO alone [18]. Spinel magnesium aluminate ($MgAl_2O_4$) is a naturally occurring and readily synthesizable nanohybrid that exhibits remarkable properties, including a melting point of 2135 °C, a hardness of 16 GPa, and a low density of 3.58 g/cm^3 [19,20]. These substantial characteristics have wide applications in AM, including industries (e.g., ceramics, cement), photocatalysis, methane production from CO2, ethanol synthesis, energy storage, hydrogen production, and adsorption [21–24]. Metal oxides are often used as additives in refractory materials due to their elevated melting points, reactive chemistry, and propensity to interact with other metal oxides, thereby enhancing the sintering capabilities of spinel materials and imparting novel characteristics [25]. Currently, researchers are focusing on simplifying synthesis processes to produce low-cost, environmentally safe sorbents.

Herein, we aimed to prepare $MgAl_2O_4$@MgO (AM) via a simplified one-pot process using dextrose as a capping agent, following an in situ protocol. Thereafter, 5%NiO-

$MgAl_2O_4$@MgO (AMNi), 5%CoO-$MgAl_2O_4$@MgO (AMCo), and 5%CuO-$MgAl_2O_4$@MgO (AMCu) nanocomposites will be prepared similarly. The fabricated AM, AMNi, AMCo, and AMCu triple nanohybrids will be characterized and tested for the removal of IDC as a pollutant. The IDC sorption parameters will be optimized, and the sorption kinetics and equilibria will be investigated. Additionally, the sorbent's reusability and suitability for use in natural water conditions will be evaluated.

2. Results and Discussion

2.1. Characterization of AM, AMCu, AMNi, and AMCo

The surface morphology of AM, AMCu, AMNi, and AMCo was examined by SEM. The captured images in Figure 1 show spherical and/or elliptical particles. The particle size was determined using the ImageJ program (Version 1.51 23 April 2018, Windows version). The AM, AMCu, AMNi, and AMCo showed size ranges of 21.6–51.4 nm, 9.8–13.8 nm, 19.1–32.2 nm, and 9.2–31.2 nm, respectively. Notably, AMCu exhibited the shortest size range and the smallest particle sizes. The narrow particle size ranges obtained with dissimilar doping ions in the AM, AMCu, AMNi, and AMCo nanocomposites may serve as a model for the general fabrication of nanoscale heterocomposites.

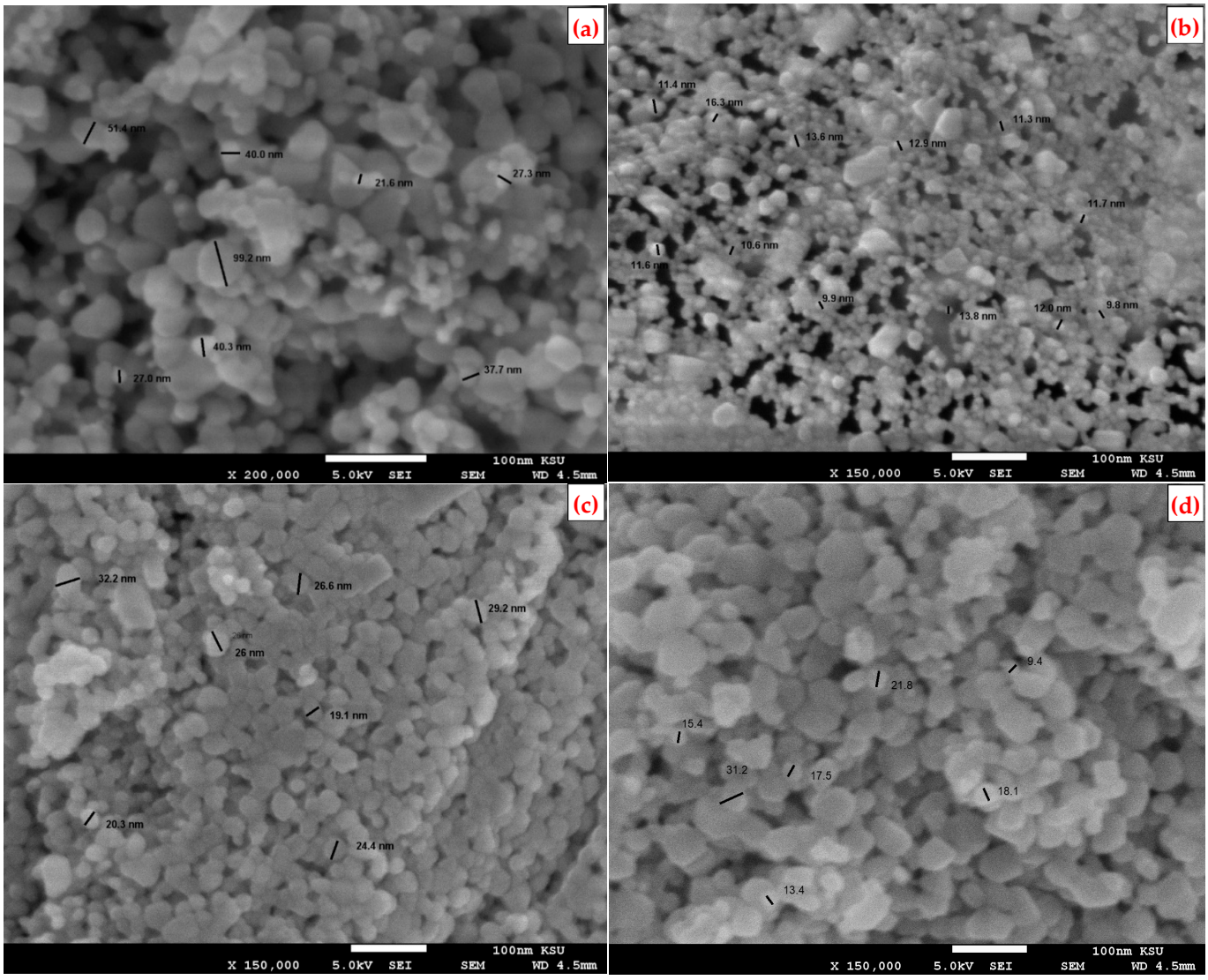


Figure 1. SEM images of (**a**) AM, (**b**) AMCu, (**c**) AMNi, and (**d**) AMCo.

The elements constituting the as-synthesized AM, AMCu, AMNi, and AMCo were identified through EDX. The obtained spectra in Figure 2a–d confirmed the presence of aluminum, oxygen, and magnesium in the synthesized AM, AMCu, AMNi, and AMCo, with intrinsic peaks of Cu, Ni, and Co appearing in the corresponding spectra of the triple composites, respectively. At the same time, Table 1 shows the ratios of the elements that compose these nanohybrids. The presented spectra and the inserted tables confirm the purity of the AM, AMCu, AMNi, and AMCo nanocomposites, at ratios close enough to the intended doping ratios. Additionally, the EDX mapping technique was employed for examining the elemental distribution homogeneity in AM, AMCu, AMNi, and AMCo (Figure 2e–h). The Cu, Ni, and Co maps showed excellent homogeneous distribution across the test areas.

Table 1. The elemental composition of AM, AMCu, AMNi, and AMCo, and the ratio of elements constituting them.

Element	AM		AMCu		AMNi		AMCo	
	Mass %	**Atomic %**	**Mass %**	**Atomic %**	**Mass %**	**Atomic %**	**Mass %**	**Atomic %**
Mg	42.19	44.09	41.29	36.95	31.73	29.40	34.48	32.63
Al	24.46	19.18	20.93	16.66	25.73	21.48	20.14	17.18
O	33.34	36.72	32.76	44.43	32.02	45.08	31.00	44.59
Cu	-	-	5.11	1.75	-	-	-	-
Ni	-	-	-	-	10.52	4.04	-	-
Co	-	-	-	-	-	-	14.38	5.61

Figure 3 depicts the X-ray spectra of AM, AMCu, AMNi, and AMCo. The diffraction peaks at 2θ° at 19.11, 31.18, 36.86, 44.74, 59.58, 65.16, 74.66, and 78.43 in the XRD patterns of AM, AMCu, AMNi, and AMCo correspond to the cubic crystal planes of $MgAl_2O_4$, namely (111), (220), (311), (400), (511), (440), (620), and (533), which showed an excellent agreement to the JCPDS 96-900-2740 as predicted via the MATCH software (Version 4.0). Furthermore, the predominant diffraction maxima at 42.78 and 62.16 2θ° can be attributed to the (200) and (220) planes of the cubic MgO crystal (JCPDS 96-900-6806), as predicted by the MATCH software (Version 4.0). The CuO, NiO, and CoO doping resulted in the phases of $CuAl_2O_4$ (JCPDS 96-900-5727), $NiAl_2O_4$ (JCPDS 96-900-6039), and $Co_{0.08}Mg_{0.91}Al_2O_4$ (JCPDS 96-901-6720) in the corresponding nanohybrids. Considering the principal XRD peaks of MgO and $MgAl_2O_4$ (about 2θ° ≈ 42.9 and 2θ° ≈ 37.0) indicated a phase ratio of 4:1, respectively. The crystal size was determined using Bragg's angles and Debye-Scherer's formula (Equation (1)). Table 2 displays the lattice dimensions (a) and imperfection (c) as calculated using Equations (2) and (3), respectively [12].

$$D = \frac{0.9\lambda}{\beta \cos\theta} \quad (1)$$

$$a = \frac{\lambda}{\sqrt{3}\, sin\theta} \quad (2)$$

$$c = \frac{\lambda}{sin\theta} \quad (3)$$

λ, D, and β symbolize the wavelength, the crystal size, and the half-height XRD peak-width. Table 2 revealed a significant shift in the D-values, accompanied by a change in the principal MgO peak (2θ = 44.236°) angle position, suggesting a lattice expansion attributed to the doping process. Furthermore, doping the AM with CuO, NiO, and CoO resulted in

reducing the crystal's lattice parameter (a) and increasing the c values, indicating a robust metal oxide–AM interaction.

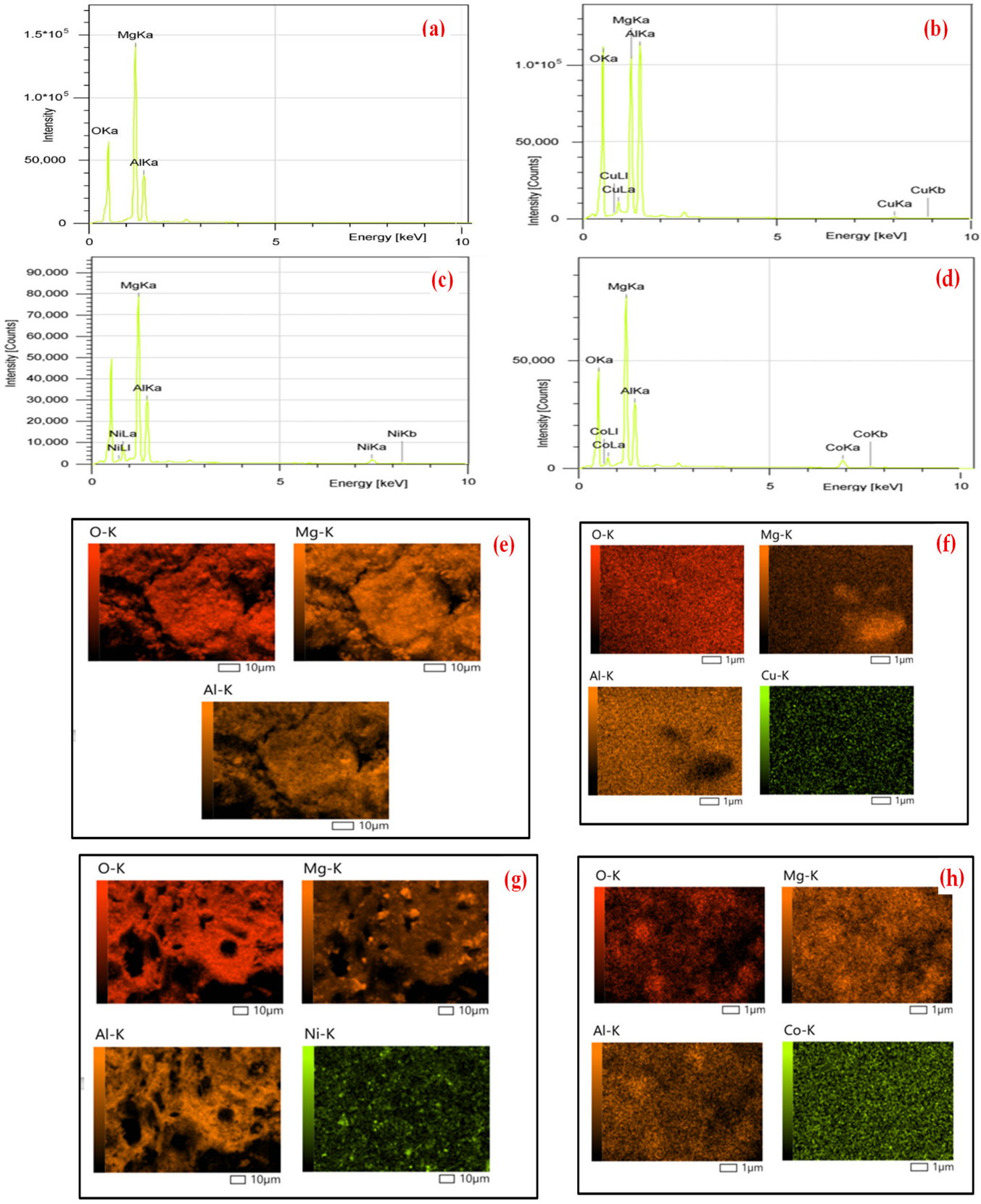


Figure 2. (**a**–**d**) show the EDX spectra of AM, AMCu, AMNi, and AMCo, respectively, while (**e**–**h**) are the elemental mapping, respectively.

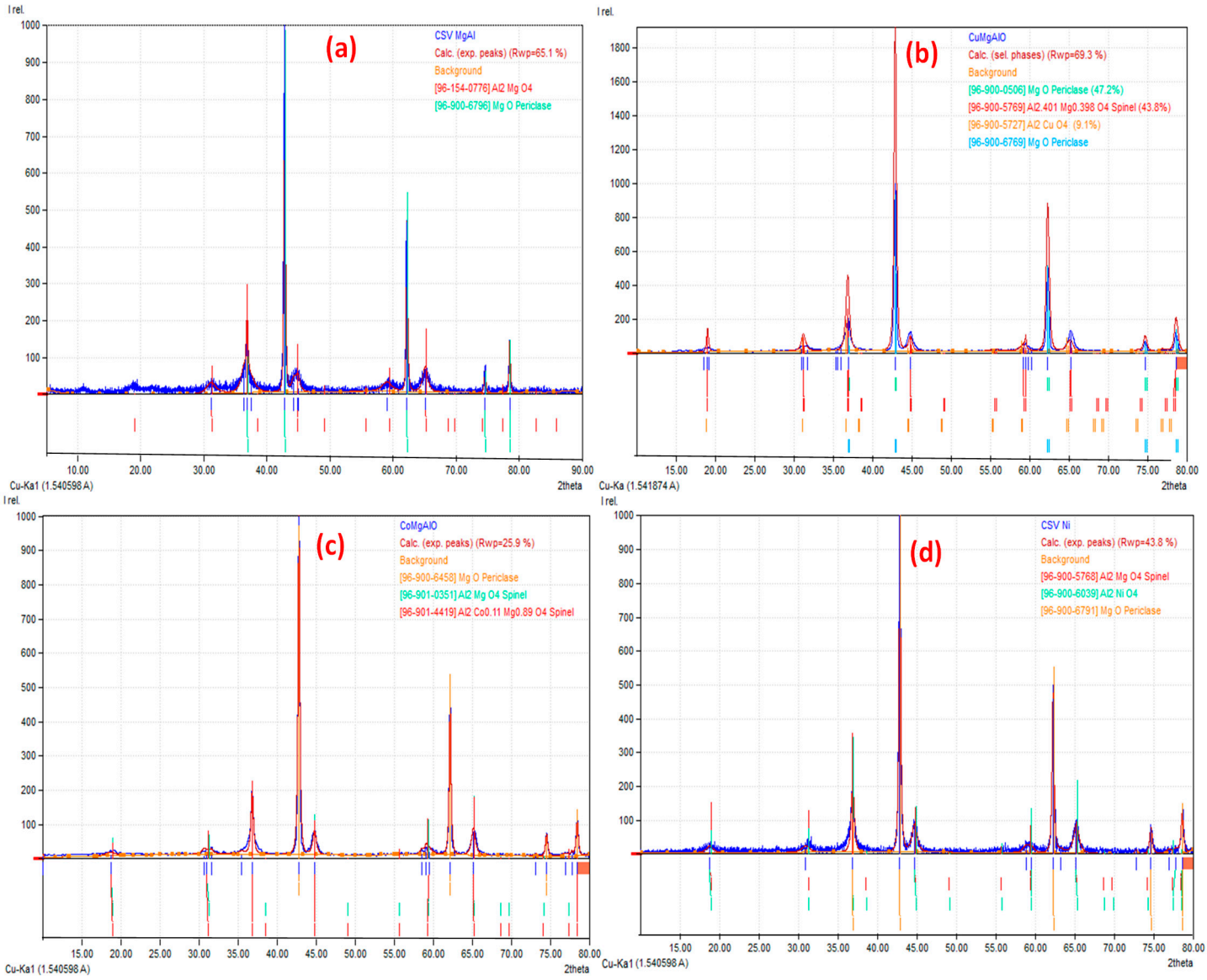


Figure 3. The XRD patterns of the prepared (**a**) AM, (**b**) AMCu, (**c**) AMCo, and (**d**) AMNi nanocomposites.

Figure 4 shows the FT-IR spectra of the AM, AMCu, AMNi, and AMCo nanocomposites. The peak about 418 cm^{-1} could be allocated to Mg-O of the MgO, while the doublet IR peaks at 839 and 698 cm-1 are attributed to asymmetric and symmetric Al-O-Al and the Mg-O-Al of spinel $MgAl_2O_4$ construction [26,27]. The 1623 cm^{-1} bands could be indicative of the O-H bending vibration, while the broad band between 3000–3500 cm^{-1} is allocatable to the hydrogen-bonded O-H stretching of adsorbed moisture on the AM, AMCu, AMNi, and AMCo surfaces [28]. The vibrating bands about 523 cm^{-1} in the AMCu, AMNi, and AMCo can be assigned to stretching vibrations of Cu-O, Ni-O, and Co-O bonds.

The surface characteristics of AM, AMCu, AMNi, and AMCo nanocomposites were surveyed using N2 adsorption–desorption (Figure 5). The isotherms of AM, AMCu, AMNi, and AMCo exhibited minimal adsorption at low pressures, with adsorption increasing with relative pressure. The AM, AMCu, AMNi, and AMCo exhibited type IV isotherms with an H3 loop-type, indicative of a mesoporous structure with bucket-like and/or cylindrically shaped pores [29–31]. The BET surface area of AM, AMCu, AMNi, and AMCo was 69.47, 95.87, 86.23, and 75.87 m^2 g^{-1}, respectively, while the average pore diameter was 126.09, 158.40, 130.96, and 131.35 Å, respectively. Compared to AM, the surface characteristics of AMCu, AMNi, and AMCo showed significant improvement. Considering that the process

was tested here using three different elements, it can be generalized that doping AM with a transition-metal oxide at the studied dose via the proposed protocol could improve AM surface properties.

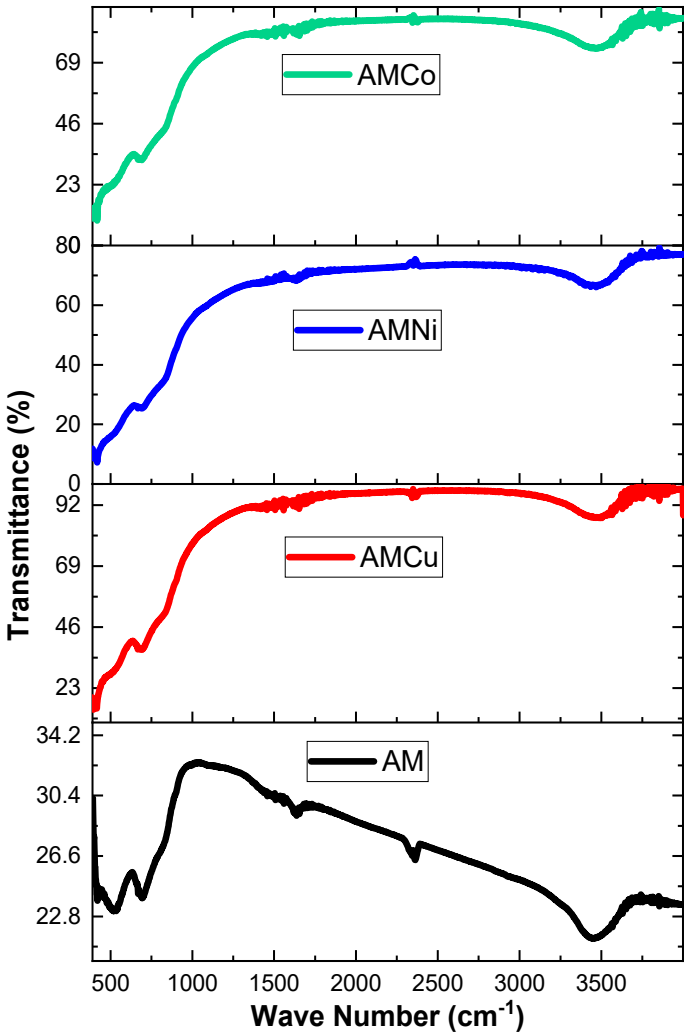


Figure 4. The FTIR spectra of AM, AMCu, AMCo, and AMNi nanocomposites.

Table 2. The XRD parameters of the prepared AM, AMCu, AMCo, and AMNi nanocomposites.

AM						**AMCu**					
Fitting R^2 = 0.979						**Fitting R^2 = 0986**					
2θ	**FWHM (β)**	**D=**	**a=**	**c=**	**ε=**	**2θ**	**FWHM (β)**	**D**	**a=**	**c=**	**ε=**
19.014	1.614	4.853	0.015	0.933	0.007	15.483	0.273	28.838	0.012	1.840	0.001
35.462	8.660	0.874	0.027	0.506	0.036	19.001	1.254	6.248	0.015	0.918	0.005
36.822	0.817	9.221	0.028	0.488	0.003	31.523	2.014	3.797	0.024	0.732	0.008
42.829	0.304	24.359	0.032	0.422	0.001	36.871	0.952	7.917	0.028	0.603	0.004
44.236	3.050	2.413	0.033	0.409	0.012	42.926	0.358	20.638	0.033	0.565	0.001
62.181	0.396	17.179	0.046	0.298	0.001	44.815	1.018	7.214	0.034	0.484	0.004
62.181	1.474	4.616	0.046	0.298	0.006	59.424	1.880	3.670	0.044	0.459	0.007
65.148	1.904	3.516	0.048	0.286	0.007	62.332	0.400	17.012	0.046	0.399	0.001
74.624	0.394	16.033	0.054	0.254	0.001	65.274	0.942	7.101	0.048	0.356	0.003
78.573	0.415	14.833	0.056	0.243	0.001	74.726	0.428	14.740	0.054	0.333	0.001
Avge	1.903	9.790	0.039	0.414	0.008	78.653	0.471	13.060	0.056	0.308	0.002

Table 2. *Cont.*

AMNi						AMCo					
Fitting R^2 = 0978						Fitting R^2 = 0.988					
2θ	FWHM	D=	a=	c=	ε=	2θ	FWHM (β)	D=	a=	c=	ε=
18.911	1.280	6.122	0.015	0.938	0.006	18.980	1.644	4.766	0.015	0.934	0.007
31.331	1.416	5.403	0.024	0.571	0.006	31.468	1.702	4.494	0.024	0.568	0.007
36.897	0.626	12.039	0.028	0.487	0.003	36.866	0.647	11.640	0.028	0.487	0.003
42.903	0.343	21.542	0.033	0.421	0.001	42.858	0.311	23.777	0.032	0.422	0.001
44.755	0.911	8.066	0.034	0.405	0.004	44.819	0.888	8.268	0.034	0.404	0.004
59.380	1.660	4.156	0.044	0.311	0.006	60.382	5.411	1.269	0.045	0.306	0.020
62.335	0.416	16.331	0.046	0.298	0.002	62.233	0.348	19.561	0.046	0.298	0.001
65.233	0.858	7.802	0.048	0.286	0.003	65.289	0.804	8.320	0.048	0.286	0.003
74.762	0.478	13.201	0.054	0.254	0.002	74.599	0.423	14.956	0.054	0.254	0.001
78.712	0.488	12.588	0.056	0.243	0.002	78.529	0.442	13.927	0.056	0.243	0.001
Avge	0.848	10.725	0.038	0.421	0.003	Avge	1.262	11.098	0.038	0.420	0.005

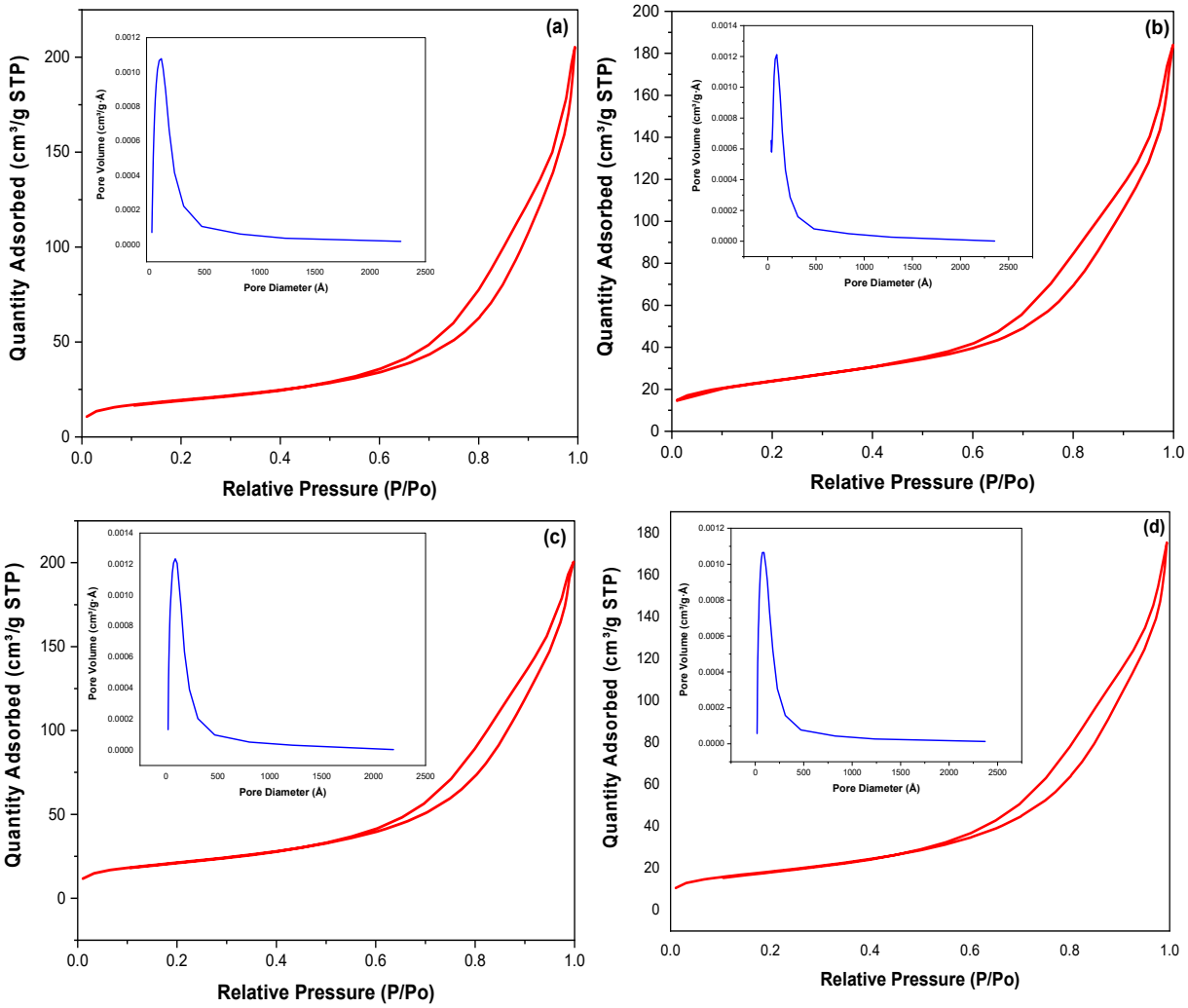


Figure 5. The N_2-sorption–desorption loops with the insert pore size distribution of (**a**) AM, (**b**) AMCu, (**c**) AMNi, (**d**) AMCo.

2.2. Contact Time and Kinetic Investigations

As a function of time, adsorption kinetics show how the adsorption process evolves. Time is a crucial metric that needs to be considered [32]. The adsorption of the IDC dye onto

AM, AMCu, AMNi, and AMCo nanocomposites was assessed using a batch method. With 50 mg of each sorbent, a 100 mL solution of IDC (100 mg L^{-1}) was stirred continuously. Afterwards, a UV-vis spectrophotometer was used to quantify the IDC concentrations after filtering a sample from each beaker using a syringe equipped with a 0.22 µm filter. Applying Equation (4), we calculated the adsorption capacity of IDC onto the sorbent at each time (t) and at equilibrium (q_t and q_e, mg g^{-1}) [33].

$$q_t = v(C_0 - C_t)/m \quad (4)$$

where v (L) represents the volume of the solution, C_o and C_t (mg L^{-1}) denote the initial and equilibrium concentrations of IDC in the solution, respectively, and m (g) indicates the mass of the adsorbent [12]. Figure 6 depicts the contact time study of IDC sorption onto AM, ACu, AMNi, and AMCo nanocomposites. The sorption on the four sorbents progressed fast and reached equilibrium within 120 min. The AM, AMCu, AMNi, and AMCo possessed q_t values of 59.55, 127.62, 87.45, and 84.55 mg g^{-1}, respectively. These results align with the AMCu having the highest surface area among the prepared nanohybrids and are consistent with the literature (Table 3). Worth noting that approximately 60% of the IDC uptake occurred within the first 40 min, with superior performance for the AMCu nanocomposites, which achieved a 214% removal efficiency compared to the base material (the AM). Figure 6a shows faster IDC removal by AMCu, AMNi, and AMCo in the early stages, which slowed down as they approached equilibrium. This can be attributed to the IDC molecules in the liquid phase being repelled from the sorbent surface, even when sorption sites are available [34].

Table 3. Comparing the AM, AMCu, AMNi, and AMCo performance in removing IDC by some literature findings.

Sorbent	q_t (mg g^{-1})	Reference
AM	59.5	This study
AMCu	127.6	This study
AMNi	87.5	This study
AMCo	84.6	This study
commercial activated carbon	79.5	[35]
Activated Leaves of Agave Americana	61.7	[36]
Brazil nut shell bioadsorbents	1.1	[37]
Rice husk ash	29.3	[37]
PVA/SiO_2 nanofiber	40.6	[37]
Graphene oxide/polyaniline nanoparticle	88.7	[37]
Graphene oxide/polyaniline/Mn_2O_3 nanoparticle	76.4	[37]
Zeolitic material	32.8	[37]
Sulfonated polystyrene	20.0	[38]
cobalt hydroxide nanoparticles	62.5	[39]
Terminalia catappa shell	26.8	[40]
Zn/Activated carbon (ACZ)	121.8	[41]
CdSe nanoparticles	103.1	[42]
C_3N_4@ MoO_3/$MgAl_2O_4$	98.2	[43]

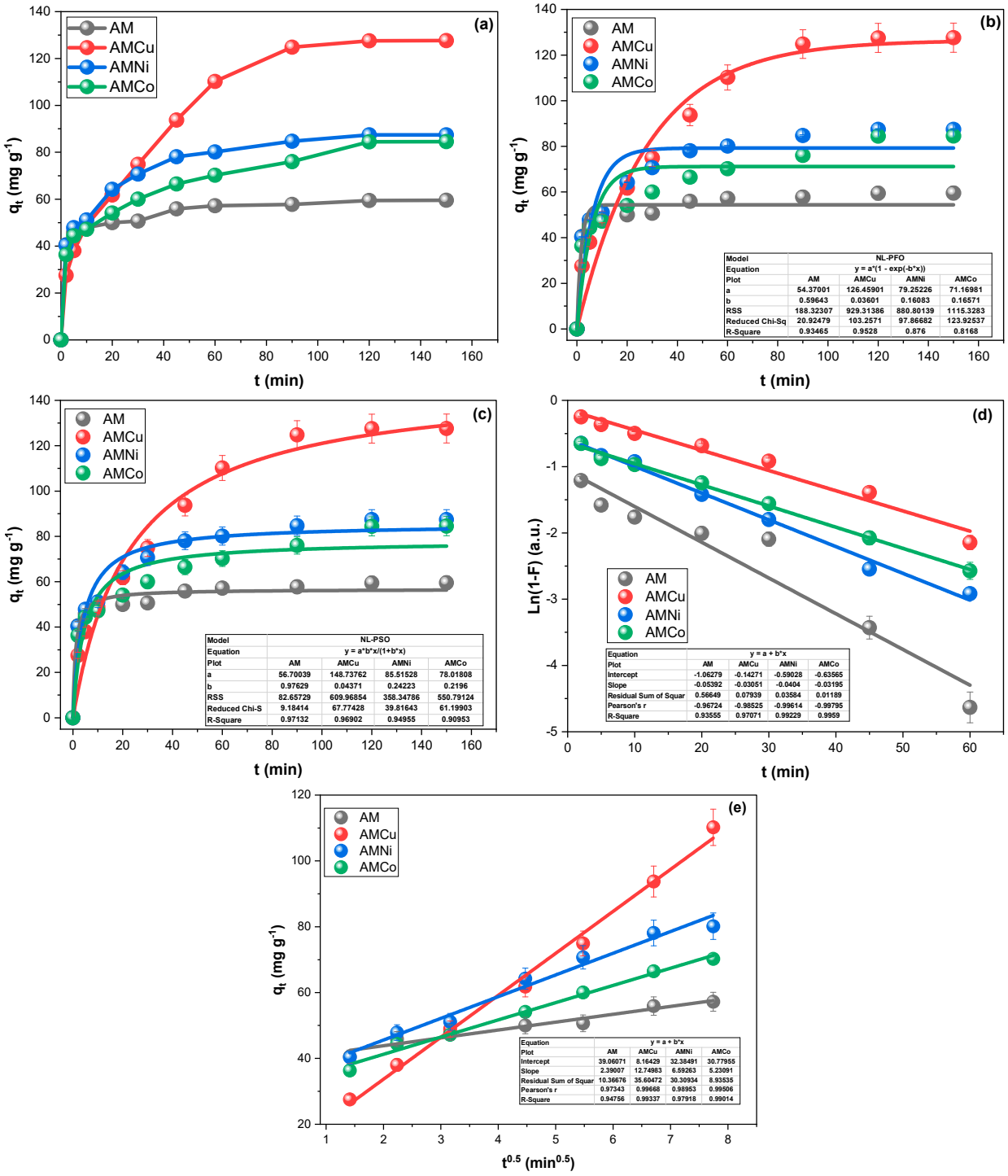


Figure 6. (**a**) contact time results, (**b**) NL-PFO, (**c**) NL-PSO, (**d**) LFDM, (**e**) IPDM plots of IDC removal by AM, AMCu, AMNi, and AMCo from 100 mg L^{-1} solution.

Furthermore, the IDC sorption rate order for its removal by the AM, AMCu, AMNi, and AMCo nanocomposites was studied using the non-linear pseudo-first-order (NL-PFO, Equation (5)) and non-linear pseudo-second-order (NL-PSO, Equation (6)) models. Additionally, the IDC sorption mechanisms were examined using the liquid film diffusion model (LFDM) and the intraparticle diffusion model (IPDM), as explained by Equations (7) and (8), respectively.

$$q_t = q_e\left(1 - exp^{-K_1 \cdot t}\right) \quad (5)$$

$$q_t = \frac{k_2 \cdot q_e^2 \cdot t}{1 + k_2 \cdot q_e \cdot t} \quad (6)$$

$$ln(1 - F) = -K_{LF} \times t \quad (7)$$

$$q_t = K_{IP} \times t^{\frac{1}{2}} + C_i \quad (8)$$

where: C_i is a factor connected to layer boundaries. k_1 (min^{-1}), k_2 (g mg^{-1} min^{-1}), k_{IP} (mg g^{-1} $min^{-1/2}$), and k_{LF} (min^{-1}) stand for NL-PFO, NL-PSO, LFDM, and IPDM constants, respectively. Figure 6b,c illustrate the NL-PFO and NL-PSO graphs from which k_1 and k_2 were calculated by substituting the slope and intercept into the corresponding parameter mathematical formula (Table 4). The correlation coefficient (R^2), along with the residual sum of squares and the reduced Chi-square, was used to assess the best-fitting model [44]. The NL-PSO showed alignment in the IDC sorption onto AM, AMCu, AMNi, and AMCo, with higher R^2 values and lower RSS and X^2 values, whereas the opposite was observed with the NL-PFO [34,45]. Furthermore, the step controlling IDC sorption onto AM, AMCu, AMNi, and AMCo was investigated. Figure 6d,e display the IPDM and LFDM plots for IDC sorption on the four sorbents, while Table 4 presents the computed results. The plots of IDC sorption onto AM, AMCu, AMNi, and AMCo nanocomposites showed R^2 values close to unity for both models; however, the nonzero intercept for the IPDM indicates that the rate-limiting step involves both IPDM and LFDM, which together influenced the IDC sorption. Therefore, the adsorption process initially involves rapid film diffusion at high initial concentrations, followed by intraparticle diffusion as adsorption proceeds [46].

Table 4. Kinetic results of IDC sorption onto AM, AMCu, AMNi, and AMCo nanocomposites.

Adsorption Rate Order											
Sorbent	**qmax Exp ($mg \cdot g^{-1}$)**	**NL-PFO**					**NL-PSO**				
		qe (mg. g^{-1})	**K_1**	**R^2**	**X^2**	**RSS**	**q_e (mg g^{-1})**	**K_2**	**R^2**	**X^2**	**RSS**
AM	84.551	54.370	0.596	0.935	20.925	188.323	56.700	0.0125	0.971	9.184	82.657
AMCu	127.622	126.459	0.036	0.953	103.257	929.314	148.738	0.0003	0.969	67.774	609.969
AMNi	87.453	79.252	0.161	0.876	97.867	880.801	85.515	0.0028	0.950	39.816	358.348
AMCo	84.551	71.170	0.166	0.817	123.925	1115.328	78.018	0.0028	0.910	61.199	550.791
Adsorption Rate Mechanism											
Sorbent	**IPDM**					**LFDM**					
	K_{IP} ($mg \cdot g^{-1}$ $min^{1/2}$)	**C (mg g^{-1})**	**R^2**	**RSS**	**K_{LF} (min^{-1})**	**R^2**	**RSS**				
Am	2.390	39.061	0.948	10.367	0.054	0.936	0.566				
AMCu	12.750	8.164	0.993	35.605	0.031	0.971	0.079				
AMNi	6.593	32.385	0.979	30.309	0.040	0.992	0.036				
AMCo	5.231	30.779	0.990	8.935	0.032	0.996	0.012				

2.3. Isotherms and Thermodynamics

The contact time results demonstrated the AMCu superiority among the tested sorbents; therefore, the impacts of temperature and IDC concentration on its sorption by AMCu were investigated (Figure 7a). The gained q_t value increases proportionately with the IDC concentration, exhibiting experimental qt values of 279.8 mg g^{-1} at a 200 mg L^{-1} concentration. The temperature dependence of IDC elimination by the AMCu was investigated (293–323 K), revealing a significant qt rise, indicating endothermic sorption. The enhanced IDC removal with elevated temperatures (Figure 7a) can be attributed

to the induced IDC mobility via liquid-phase diffusion and/or the swelling of the AMCu particle's internal structure, which facilitates the infiltration of IDC into the porous framework of the AMCu. This could also be interpreted as a consequence of the AMCu particle's disintegration, exposing new sorption sites [47]. Given such a high q_t value, this quality is essential in the real world, where frequent temperature changes and the need to maintain high removal efficiency are common [48].

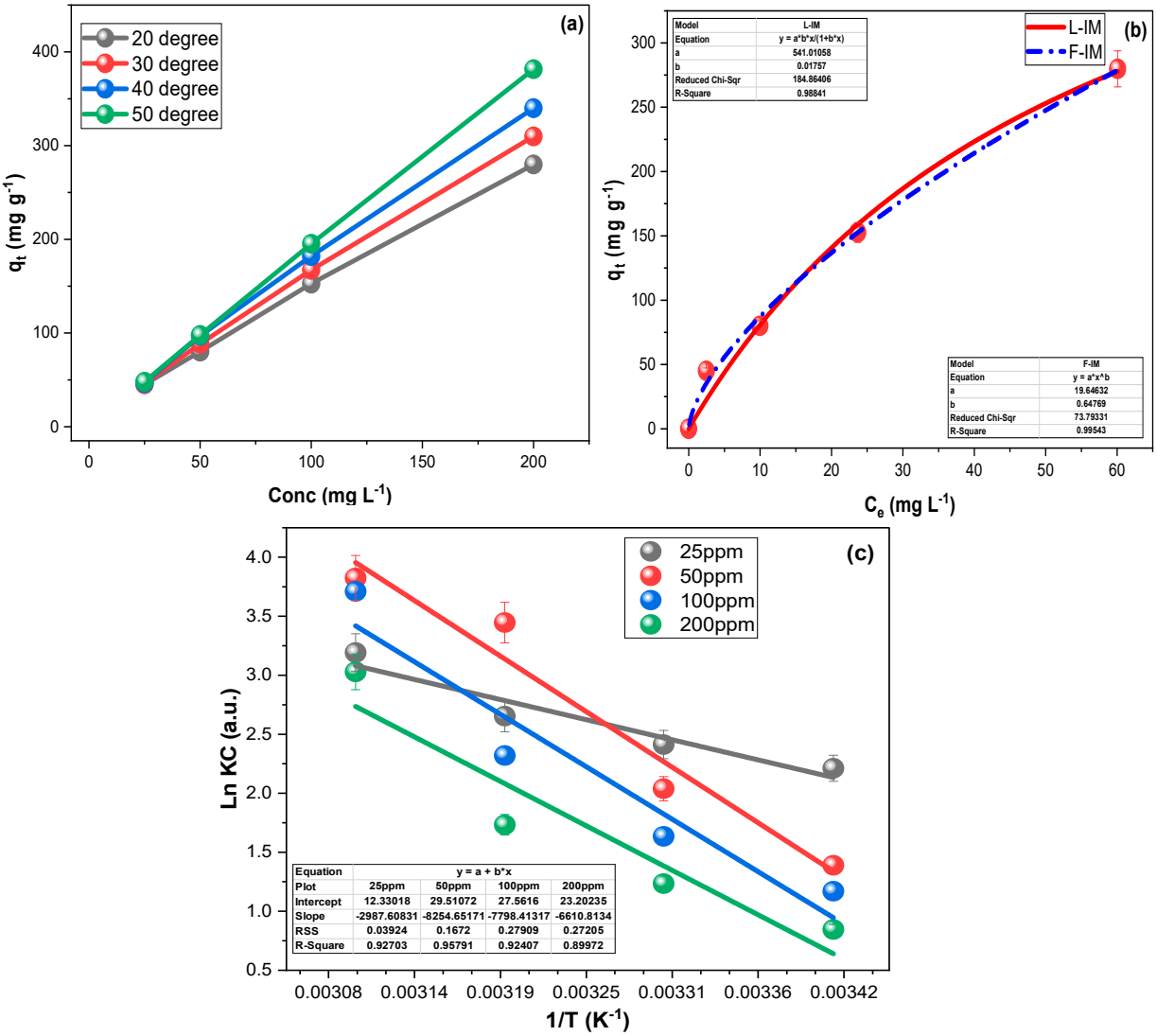


Figure 7. (**a**) Effect of concentration and temperature on IDC sorption from 25 to 200 mg L^{-1} concentration range and 293 to 323 K, (**b**) L-IM and F-IM fittings, and (**c**) thermodynamic plot from the above-identified concentration and temperature ranges at pH = 6.0.

The most popular models, the Langmuir (L-IM) and the Freundlich (F-IM) isotherms, were applied to explain IDC sorption onto AMCu [49]. L-IM (Equation (9)) was employed to test the one-layer IDC sorption possibility without IDC-AMCu interaction, while the multiple-layer IDC sorption was tested via F-IM (Equation (10)).

$$q_e = \left(\frac{K_l q_e C_e}{1 + q_e C_e} \right) \tag{9}$$

$$q_e = K_F \cdot C_e^{\frac{1}{n}} \tag{10}$$

where: C_e (mg L^{-1}) denotes the IDC concentration in the solution at equilibrium; q_e represents the maximum q_t; K_L (L mg^{-1}) is the L-IM constant; K_F (L g^{-1}) and 1/n signify the F-IM constant and the favorability factor, respectively [12,50]. Figure 7b displays the combined L-IM and F-IM non-linear plots of IDC adsorption on AMCu, with the findings of the two models outlined in Table 5. The fitting results demonstrated that IDC sorption onto AMCu was better described by the F-IM model, with an R^2 value of 0.995, indicating heterogeneous multilayered IDC sorption. The sub-unity value of 1/n suggested a favorable IDC sorption onto AMCu [51].

Table 5. Isotherm results of IDC sorption by MACu using concentrations ranged from 25 to 200 mg L^{-1} at 293 K, and the thermodynamic results of 25 to 200 mg L^{-1} IDC concentrations at 293, 303, 313, and 323 K.

Adsorption Isotherms							
Isotherm model →		**Langmuir**			**Freundlich**		
Temperature	**R^2**	**KL (L mg^{-1})**	**qm (g mg^{-1})**	**R^2 (a.u)**	**Kf (L g^{-1})**	**1/n (a.u)**	
293 K	0.98841	0.0116	541.01	0.99543	9.4460	0.50199	
Thermodynamic Results							
Conc. (mg L^{-1})	**ΔH° (kJ mol^{-1})**	**ΔS° (kJ mol^{-1})**	**ΔG° (293 K) (kJ mol^{-1})**	**ΔG° (303 K) (kJ mol^{-1})**	**ΔG° (313 K) (kJ mol^{-1})**	**ΔG° (323 K) (kJ mol^{-1})**	**R^2 (a.u)**
25.0	+24.840	+0.103	−5.198	−6.223	−7.248	−8.273	0.927
50.0	+68.633	+0.245	−3.259	−5.713	−8.167	−10.620	0.958
100.0	+64.840	+0.229	−2.304	−4.596	−6.887	−9.179	0.924
200.0	+54.966	+0.193	−1.559	−3.488	−5.417	−7.346	0.899

The thermodynamics of the IDC sorption onto AMCu can be assessed using characteristic thermodynamic parameters, including the Gibbs free energy (ΔG°), enthalpy (ΔH°), and entropy (ΔS°). Kc was computed via Equation (11), then ln(Kc) was plotted versus the reciprocal of absolute temperature (1/T, 1/K) (Equation (12)), and the application of the resulting ΔH° and ΔS° in Equation (13) [52,53].

$$K_c = \frac{IDC\ adsorbed\ concentration\ at\ equilibrium}{IDC\ unadsorbed\ concentration\ at\ equilibrium} \quad (11)$$

$$lnK_c = \frac{\Delta H^\circ}{RT} + \frac{\Delta S^\circ}{R} \quad (12)$$

$$\Delta G^\circ = \Delta H^\circ - T\,\Delta S^\circ \quad (13)$$

where: K_C (a.u) is the equilibrium constant, T (K) is the IDC sorption temperature, R = 0.0081345 (kJ mol^{-1}) is the ideal gas constant [54]. The positive ΔH° shown in Table 5 indicates an endothermic IDC sorption onto AMCu, while the negative ΔG° values indicate the spontaneity of IDC sorption onto AMCu at the studied temperature ranges. Furthermore, the positive ΔS° value of IDC sorption onto AMCu indicated a less disordered solid–liquid interface [55].

2.4. The pH Impact on IDC Sorption by AMCu

Solution pH is a crucial controlling parameter in sorption processes, as it can affect the sorbent surface charge and the ionization of sorbate groups, if any. The pH effect on IDC sorption onto AMCu was studied, illustrating a greater favourability for acidic media (pH = 2.0 to 6.0) compared to higher pH levels, where the q_t values decreased substantially as the pH was raised (Figure 8a). The IDC sorption showed a steady rise from pH 2.0 to 6.0, revealing a q_t range of 70.46 and 155.20 mg g^{-1} [56]. Although the maximum IDC sorption occurred in a neutral medium (pH 7.0), mildly acidic media (pH 5–6) are still

suitable for this process. Thanks to the abundance of H+ ions between pH 2.0 and 6.0, the AMCu surface is expected to be positively charged, leading to electrostatic attraction of IDC molecules via their electron-rich functional groups. The decreased IDC sorption as the solution's pH increased could be attributed to the accumulation of the highly available OH anion on the AMCu surface, leading to repulsion of the IDC molecules through their electronegative sites. In conclusion, to achieve acceptable IDC removal, it is recommended to maintain a pH between 4.0 and 8.0 [57].

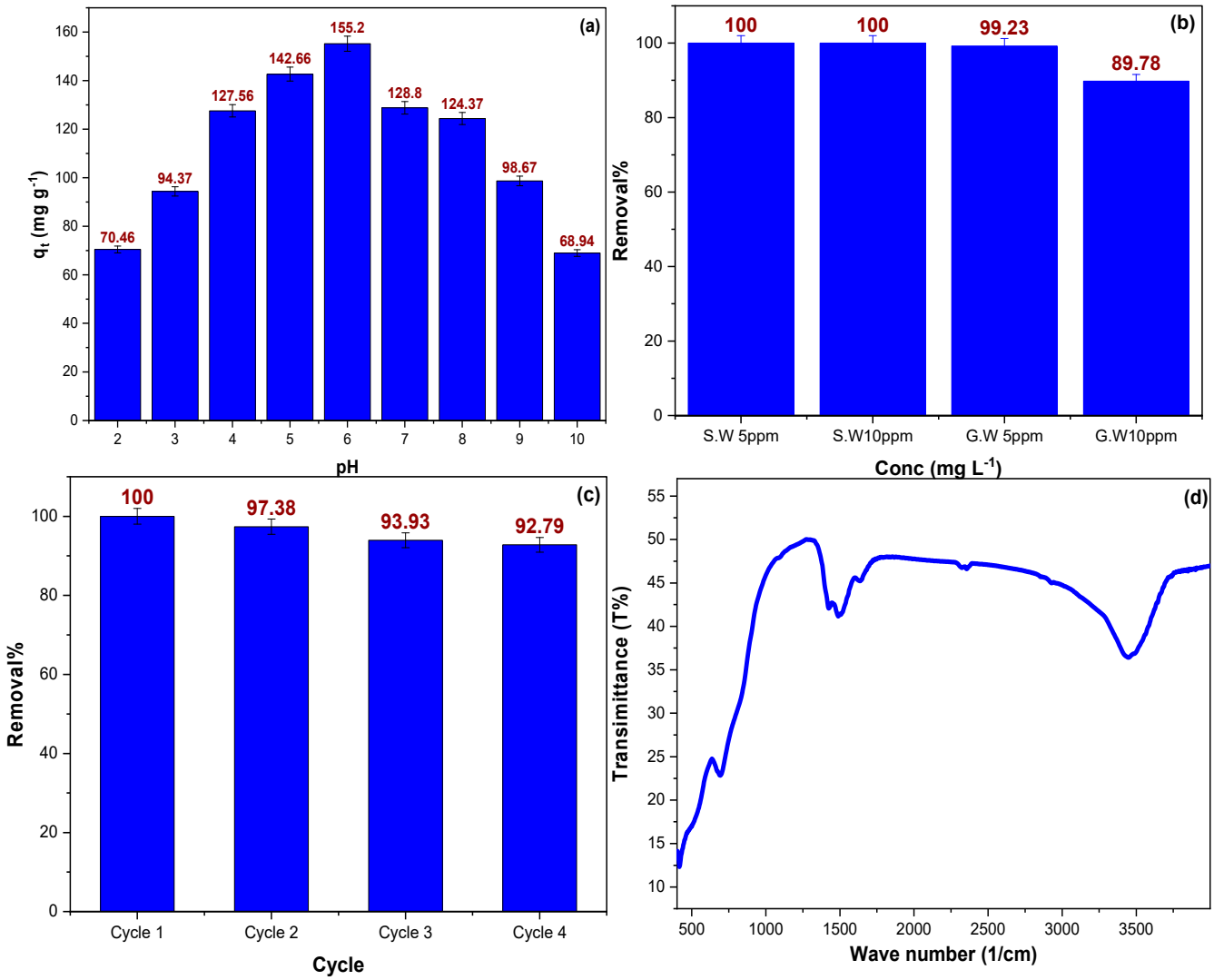


Figure 8. (**a**) illustrates the effect of pH on the sorption of IDC onto AMCu, (**b**) demonstrates the application of AMCu in the decontamination of natural water samples spiked with IDC at concentrations of 5 and 10 mg L^{-1}, and (**c**) the regeneration and reusability outcomes of AMCu, (**d**) the FTIR analysis of the regenerated AMCu nanohybrid.

2.5. Application to Natural Water and Reusability Studies

A Seawater (SEAW) sample and a groundwater (GRW) sample were employed as solvents for preparing IDC at concentrations of 5 and 10 mg L^{-1}. The 5 and 10 mg L^{-1} concentrations were used as low values sufficient to test the adsorbent's capability but high enough to be quantified without being too low to compromise accuracy. The SEAW samples were collected from the Red Sea at Jeda, while the GRW samples were collected from Sudair Industrial City, Riyadh. The SEAW and GEW showed TDS values of 36.14 and 0.37 g L^{-1}, respectively, and temperatures of 25.5 °C and 25.7 °C, respectively. The solutions were then adjusted to pH 6.0. For both samples, 120 mL of each solution was stirred with

50 mg of AMCu sorbent for 2.0 h, after which sorption efficiencies were computed. Figure 8b displays the results of the AMCu effectiveness for eliminating IDC. The slightly lower IDC removal rate from SEAW compared to GRW may be due to the higher salt concentration in SEAW, which could block some of the active sorption sites on AMCu and/or hinder the diffusion of IDC solution to the AMCu surface.

The reusability of the AMCu nanocomposite was investigated over four consecutive cycles (Figure 8c). The nanocomposite's effectiveness in IDC sorption was confirmed in a four-cycle study, in which the reused AMCu showed minimal changes in adsorption percentage. Its ability to be reused four times without performance loss indicates robust efficiency and performance stability. The stability of the reused AMCu has been tested by conducting FTIR analysis of the adsorbent (Figure 8d). The obtained peaks matched those observed with the virgin AMCu, except for the OH peak enlargement with the reused AMCu, which is attributable to adsorbed moisture and/or the conversion of a portion of AMCu to hydroxides.

3. Materials and Methods

3.1. Materials

Aluminum chloride ($AlCl_3 \cdot 6H_2O$, Sigma Aldrich) was obtained from the St. Louis, MO, USA. Magnesium chloride ($MgCl_2 \cdot 6H_2O$, Riedel-de Haën, Seelze, Duitsland) and Dextrose anhydrous (DXT, Riedel-de Haën) were sourced from Hannover, Germany. Nickel acetate (Fluka, Seelze, Germany) and indigo carmine (IDC, Fluka) were purchased from Buchs, Switzerland. Copper nitrate trihydrate ($Cu(NO_3)_2 \cdot 3H_2O$, Win-Lab, North Brunswick Township, NJ, USA) and anhydrous cobalt acetate ($Co(CH_3COO)_2$, Win-Lab) were obtained from London, England.

3.2. Preparation of Magnesium Aluminate Nanohybrids

Exact amounts of 0.1 mol of $MgCl_2 \cdot 6H_2O$, 0.05 mol of $AlCl_3 \cdot 6H_2O$, 200 mL of distilled water, and 5.0 g of DXT, which serves as a reducing and stabilizing agent, were placed into a 500 mL beaker, which was then heated by a hotplate at 200 °C until dryness. The one-pot constituents were converted into a black, solid product, ground, calcined at 550 °C for 5.0 h, and then the AM was collected. The AMNi, AMCo, and AMCu were prepared by adding nickel acetate, copper nitrate, and cobalt acetate to the one-pot composition prior to heating, and the beakers were then heated under the same AM synthesis conditions.

3.3. Characterization

The AM, AMNi, AMCo, and AMCu triple nanohybrids were tested via scanning electron microscopy (SEM, JSM-IT500, Tokyo, Japan), X-ray diffraction (Bruker AXS, Karlsruhe, Germany), Fourier transform infrared spectroscopy (FTIR, Tracer100, Tokyo, Japan), and a surface analyzer (ASAP 2020, Micromeritics, Miami, FL, USA). The Shimadzu spectrophotometer (2600i, UV-vis, Tokyo, Japan) was employed to measure the sample's absorption.

3.4. IDC Adsorption

A 100 mg L^{-1} IDC solution was prepared by dissolving 100 mg of IDC in 1.0 L of DW. To investigate the adsorption of IDC on the synthesized nanohybrids, 100 mL of a 100 mg L^{-1} IDC solution containing 50 mg of each sorbent was agitated in a shaker at 150 rpm for 120 min. A Shimadzu UV-2600i spectrophotometer was used to measure absorbance at 210 nm after portions of the sample were filtered through a 0.22 µm syringe filter at specified intervals. The influence of pH on sorbents' effectiveness in removing IDC was evaluated over the pH range 2–10. An extra IDC volume was suited to the intended pH, with the excess left in the solution to account for the pH-dependent color change in the

IDC. The impact of the IDC feed concentration on its removal was tested at 25, 50, 100, and 200 mg L^{-1}. Also, the prior experiment was conducted between 20 and 50 °C to see how temperature affected IDC sorption.

To prepare the AMCu nanocomposite for reuse, it was filtered under vacuum using a 0.45 μm nylon filter, washed with ethanol and distilled water, and then dried at 110 °C for 2.0 h. Under the same conditions, second-adsorption tests were conducted on the dried AMCu nanocomposite, and its performance was compared with that of the virgin AMCu. The reusability of the AMCu nanocomposites was evaluated over four cycles. The IDC adsorption percentage of the AMCu nanocomposite was plotted as a function of cycle number.

4. Conclusions

Herin MA, AMCu, AMNi, and AMCo were synthesized using a straightforward method. Nitrogen sorption–desorption, FTIR, XRD, and SEM-EDX characterization were performed on the four nanocomposites. The AM, AMCu, AMNi, and AMCo showed type IV isotherm curves with a type H3 hysteresis loop, indicating mesoporous characteristics. The BET surface areas were 69. 69.47, 95. 87, 86. 86.23, and 75. 87 m^2 g^{-1} for AM, AMCu, AMNi, and AMCo, respectively. FTIR spectra showed distinct peaks of M-O bonds, along with peaks associated with O-H of adsorbed water. The IDC sorptions on AM, AMCu, AMNi, and AMCo were better modeled with the NL-PSO model. The LFDM controlled the IDC sorption on AMNi and AMCo, whereas the IPDM controlled its sorption on AM and AMCu. The AMCu was identified as the best sorbent for seawater and groundwater studies because it exhibited the highest adsorption capacity, reaching 127 mg g^{-1} within 120 min at a pH of 6.0. The IDC sorption onto AMCu matched that of the F-IM, which may explain the high qt value obtained with AMCu. The sorption increases with the temperature, indicating an endothermic IDC sorption onto the AMCu, and the obtained ΔG° implied that the IDC sorption onto the AMCu was spontaneous, highlighting the most effective sorbent. Both 5.0 and 10.0 mg L^{-1} IDC concentrations in natural water samples were treated by AMCu, which showed 100.0% efficacy for both groundwater samples; however, its efficacies toward the 5 and 10 mg L^{-1} IDC in seawater were 99.23% and 89.78%, respectively. The MACu's efficiency throughout four reuse cycles decreased by approximately 7.21%, demonstrating excellent performance stability.

Author Contributions: Conceptualization, M.R.E. and B.Y.A.; Methodology, S.H.E.; Validation, F.K.A.; Formal analysis, S.H.E. and M.S.; Investigation, S.H.E., M.S.E. and M.S.; Data curation, S.H.E., T.G.I. and M.S.; Writing—original draft, T.G.I. and F.K.A.; Writing—review & editing, M.R.E. and B.Y.A.; Supervision, M.R.E., F.K.A. and M.S.E. All authors have read and agreed to the published version of the manuscript.

Funding: This work was supported and funded by the Deanship of Scientific Research at Imam Mohammad Ibn Saud Islamic University (IMSIU) (grant number IMSIU-DDRSP2602).

Institutional Review Board Statement: Not applicable.

Informed Consent Statement: Not applicable.

Data Availability Statement: The original contributions presented in this study are included in the article. Further inquiries can be directed to the corresponding author.

Conflicts of Interest: The authors declare that they have no conflicts of interest.

References

1. Davoudi, S. Adsorption of methylene blue (MB) dye using NiO-SiO_2NPs synthesized from aqueous solutions: Optimization, kinetic and equilibrium studies. *Iran. J. Chem. Chem. Eng.* **2022**, *41*, 2343–2357.
2. Kgatle, M.; Sikhwivhilu, K.; Ndlovu, G.; Moloto, N. Degradation kinetics of methyl orange dye in water using trimetallic Fe/Cu/Ag nanoparticles. *Catalysts* **2021**, *11*, 428. [CrossRef]
3. Jenck, J.F.; Agterberg, F.; Droescher, M.J. Transitioning the chemical industry: The case for addressing the climate, toxics, and plastics crises. *Environ. Sci. Policy Sustain. Dev.* **2021**, *63*, 4–15. [CrossRef]
4. Jenck, J.F.; Agterberg, F.; Droescher, M.J. Products and processes for a sustainable chemical industry: A review of achievements and prospects. *Green Chem.* **2004**, *6*, 544–556. [CrossRef]
5. Al-Farraj, E.S.; Abdelrahman, E.A. Efficient photocatalytic degradation of congo red dye using facilely synthesized and characterized $MgAl_2O_4$ nanoparticles. *ACS Omega* **2024**, *9*, 4870–4880. [CrossRef]
6. Adam, F.A. Influence of doping-ion-type on the characteristics of Al_2O_3-based nanocomposites and their capabilities of removing indigo carmine from water. *Inorganics* **2022**, *10*, 144. [CrossRef]
7. Tiotsop Kuete, I.H.; Tchuifon, R.D.T.; Bopda, A.; Ngakou, C.S.; Nche, G.N.-A.; Anagho, S.G. Adsorption of indigo carmine onto chemically activated carbons derived from the Cameroonian agricultural waste garcinia cola nut shells and desorption studies. *J. Chem.* **2022**, *2022*, 1236621. [CrossRef]
8. El-Kammah, M.; Elkhatib, E.; Gouveia, S.; Cameselle, C.; Aboukila, E. Cost-effective ecofriendly nanoparticles for rapid and efficient indigo carmine dye removal from wastewater: Adsorption equilibrium, kinetics and mechanism. *Environ. Technol. Innov.* **2022**, *28*, 102595. [CrossRef]
9. Sánchez-Rodríguez, S.; Trujillo-Reyes, J.; Gutiérrez-Segura, E.; Solache-Ríos, M.; Colín-Cruz, A. Removal of indigo carmine by a Ni nanoscale oxides/*Schoenoplectus acutus* composite in batch and fixed bed column systems. *Sep. Sci. Technol.* **2015**, *50*, 1602–1610. [CrossRef]
10. Ahmad, M.B.; Soomro, U.; Muqeet, M.; Ahmed, Z. Adsorption of Indigo Carmine dye onto the surface-modified adsorbent prepared from municipal waste and simulation using deep neural network. *J. Hazard. Mater.* **2021**, *408*, 124433. [CrossRef] [PubMed]
11. Gupta, T.; Ansari, K.; Lataye, D.; Kadu, M.; Khan, M.A.; Mubarak, N.M.; Garg, R.; Karri, R.R. Adsorption of Indigo Carmine Dye by Acacia nilotica sawdust activated carbon in fixed bed column. *Sci. Rep.* **2022**, *12*, 15522. [CrossRef] [PubMed]
12. Almufarij, R.S.; Abdulkhair, B.Y.; Salih, M. Fast-simplistic fabrication of MoO_3@ Al_2O_3-MgO triple nanocomposites for efficient elimination of pharmaceutical contaminants. *Results Chem.* **2024**, *7*, 101281. [CrossRef]
13. Wang, F.Y.; Wang, H.; Ma, J.W. Adsorption of cadmium (II) ions from aqueous solution by a new low-cost adsorbent—Bamboo charcoal. *J. Hazard. Mater.* **2010**, *177*, 300–306. [CrossRef]
14. Nitha, T.; Britto, S. $MgAl_2O_4$ nanospinel: Green synthesis, characterization and effective heterogeneous catalyst for the photocatalytic degradation of carbol fuchsin dye and synthesis of 2-aryl substituted benzoxazole derivatives. *Inorg. Chem. Commun.* **2024**, *159*, 111776. [CrossRef]
15. Salih, M.; Abdulkhair, B.Y.; Alotaibi, M. Insight into the Adsorption Behavior of Carbon Nanoparticles Derived from Coffee Skin Waste for Remediating Water Contaminated with Pharmaceutical Ingredients. *Chemistry* **2023**, *5*, 1870–1881. [CrossRef]
16. Pachiyappan, J.; Gnanansundaram, N.; Sivamani, S.; Sankari, N.P.B.P.; Senthilnathan, N.; Kerga, G.A. Preparation and characterization of magnesium oxide nanoparticles and its application for photocatalytic removal of rhodamine B and methylene blue dyes. *J. Nanomater.* **2022**, *2022*, 6484573. [CrossRef]
17. Mudd, G.M. Assessing the availability of global metals and minerals for the sustainable century: From aluminium to zirconium. *Sustainability* **2021**, *13*, 10855. [CrossRef]
18. Carnes, C.L.; Kapoor, P.N.; Klabunde, K.J.; Bonevich, J. Synthesis, characterization, and adsorption studies of nanocrystalline aluminum oxide and a bimetallic nanocrystalline aluminum oxide/magnesium oxide. *Chem. Mater.* **2002**, *14*, 2922–2929. [CrossRef]
19. Ganesh, I. A review on magnesium aluminate ($MgAl_2O_4$) spinel: Synthesis, processing and applications. *Int. Mater. Rev.* **2013**, *58*, 63–112. [CrossRef]
20. Bromiley, G.D.; Nestola, F.; Redfern, S.A.; Zhang, M. Water incorporation in synthetic and natural $MgAl_2O_4$ spinel. *Geochim. Cosmochim. Acta* **2010**, *74*, 705–718. [CrossRef]
21. Almahmoud, S.A.; Alzahrani, S.S.; Abdulkhair, B.Y. Efficacious Removal of Organic Contaminants from Water Using a Novel CoO–NiO@ $MgAl_2O_4$ Nanocomposite. *ACS Omega* **2025**, *10*, 11188–11201. [CrossRef]
22. Wu, Q.; Feng, G.; Jiang, F.; Zhang, X.; Xu, Y.; Liu, J.; Liang, J.; Lao, X.; Guo, Z. Insight into enhanced adsorption of Congo red by petal-like $MgAl_2O_4$: Effect of dehydroxylation. *J. Phys. Chem. Solids* **2025**, *197*, 112398. [CrossRef]
23. Kumar, K.G.; Bhargav, P.B.; Aravinth, K.; Ahmed, N.; Balaji, C. Photoluminescence and electrochemical performance evaluation of Eu^{3+} doped $MgAl_2O_4$ phosphors for LED and energy storage applications. *Ceram. Int.* **2022**, *48*, 36038–36045. [CrossRef]

24. Abdulkhair, B.Y.E.; Ibrahim, M.N.A.E.-H.; Omran, M.K. Nanocomposite of Graphitic C_3N_4, MnO_2, and $MgAl_2O_4$ for Hydrogen Generation. U.S. Patent No. 12,365,586, 22 July 2025.
25. Zan, W.; Ma, B.; Tang, J.; Liu, K.; Cao, Y.; Tian, J.; Jiang, Z. Preparation and properties of $MgAl_2O_4$ spinel ceramics by double-doped CeO_2 and La_2O_3. *Ceram. Int.* **2023**, *49*, 15164–15175. [CrossRef]
26. Milani, S.S.; Kakroudi, M.G.; Vafa, N.P.; Rahro, S.; Behboudi, F. Synthesis and characterization of $MgAl_2O_4$ spinel precursor sol prepared by inorganic salts. *Ceram. Int.* **2021**, *47*, 4813–4819. [CrossRef]
27. Mahmoud, S.A.; Elsisi, M.E.; Mansour, A.F. Synthesis and electrochemical performance of α-Al_2O_3 and M-Al_2O_4 spinel nanocomposites in hybrid quantum dot-sensitized solar cells. *Sci. Rep.* **2022**, *12*, 17009. [CrossRef]
28. Thommes, M.; Kaneko, K.; Neimark, A.V.; Olivier, J.P.; Rodriguez-Reinoso, F.; Rouquerol, J.; Sing, K.S.W. Physisorption of gases, with special reference to the evaluation of surface area and pore size distribution (IUPAC Technical Report). *Pure Appl. Chem.* **2015**, *87*, 1051–1069. [CrossRef]
29. Bekele, E.A.; Korsa, H.A.; Desalegn, Y.M. Electrolytic synthesis of γ-Al_2O_3 nanoparticle from aluminum scrap for enhanced methylene blue adsorption: Experimental and RSM modeling. *Sci. Rep.* **2024**, *14*, 16957. [CrossRef]
30. Marcì, G.; Palmisano, L. *Heterogeneous Photocatalysis: Relationships with Heterogeneous Catalysis and Perspectives*; Elsevier: Amsterdam, The Netherlands, 2019.
31. Song, S.; Liu, Z.; Zhang, J.; Jiao, C.; Ding, L.; Yang, S. Synthesis and adsorption properties of novel bacterial cellulose/graphene oxide/attapulgite materials for Cu and Pb Ions in aqueous solutions. *Materials* **2020**, *13*, 3703. [CrossRef] [PubMed]
32. Moussout, H.; Ahlafi, H.; Aazza, M.; Maghat, H. Critical of linear and nonlinear equations of pseudo-first order and pseudo-second order kinetic models. *Karbala Int. J. Mod. Sci.* **2018**, *4*, 244–254. [CrossRef]
33. Markeb, A.A.; Moral-Vico, J.; Sánchez, A.; Font, X. Novel nanocomposite synthesis of carboxymethyl cellulose coated to zero-valent iron supported on chitosan for simultaneous removal of heavy metals and pesticides in water: Performance and mechanism. *Results Chem.* **2025**, *13*, 102041. [CrossRef]
34. Benmessaoud, A.; Nibou, D.; Mekatel, E.H.; Amokrane, S. A comparative study of the linear and non-linear methods for determination of the optimum equilibrium isotherm for adsorption of Pb^{2+} ions onto Algerian treated clay. *Iran. J. Chem. Chem. Eng. (IJCCE)* **2020**, *39*, 153–171.
35. Harrache, Z.; Abbas, M.; Aksil, T.; Trari, M. Thermodynamic and kinetics studies on adsorption of Indigo Carmine from aqueous solution by activated carbon. *Microchem. J.* **2019**, *144*, 180–189. [CrossRef]
36. Ben Nasr, J.; Ghorbal, A. Adsorption of Indigo Carmine dye onto physicochemical-activated leaves of *Agave americana* L. *Iran. J. Chem. Chem. Eng.* **2021**, *40*, 1054–1066.
37. Chowdhury, M.F.; Khandaker, S.; Sarker, F.; Islam, A.; Rahman, M.T.; Awual, M.R. Current treatment technologies and mechanisms for removal of indigo carmine dyes from wastewater: A review. *J. Mol. Liq.* **2020**, *318*, 114061. [CrossRef]
38. De León-Condés, C.A.; Roa-Morales, G.; Martínez-Barrera, G.; Menchaca-Campos, C.; Bilyeu, B.; Balderas-Hernández, P.; Ureña-Núñez, F.; Toledo-Jaldin, H.P. Sulfonated and gamma-irradiated waste expanded polystyrene with iron oxide nanoparticles, for removal of indigo carmine dye in textile wastewater. *Heliyon* **2019**, *5*, e02071. [CrossRef] [PubMed]
39. Zolgharnein, J.; Rastgordani, M. Optimization of simultaneous removal of binary mixture of indigo carmine and methyl orange dyes by cobalt hydroxide nano-particles through Taguchi method. *J. Mol. Liq.* **2018**, *262*, 405–414. [CrossRef]
40. Hevira, L.; Ighalo, J.O.; Zein, R. Biosorption of indigo carmine from aqueous solution by *Terminalia catappa* shell. *J. Environ. Chem. Eng.* **2020**, *8*, 104290. [CrossRef]
41. Odogu, A.N.; Daouda, K.; Keilah, L.P.; Tabi, G.A.; Rene, L.N.; Nsami, N.J.; Mbadcam, K.J. Effect of doping activated carbon based *Ricinodendron heudelotti* shells with AgNPs on the adsorption of indigo carmine and its antibacterial properties. *Arab. J. Chem.* **2020**, *13*, 5241–5253. [CrossRef]
42. Chikate, R.C.; Kadu, B.S. Improved photocatalytic activity of CdSe-nanocomposites: Effect of Montmorillonite support towards efficient removal of Indigo Carmine. *Spectrochim. Acta Part A Mol. Biomol. Spectrosc.* **2014**, *124*, 138–147. [CrossRef]
43. Omran, M.K.A.F.; Abdulkhair, B.Y.E. Water Decontamination via C_3N_4@ $MoO_3/MgAl_2O_4$ Nanocomposite. U.S. Patent No. 12,479,741, 25 November 2025.
44. Elamin, M.R.; Abdulkhair, B.Y.; Algethami, F.K.; Khezami, L. Linear and nonlinear investigations for the adsorption of paracetamol and metformin from water on acid-treated clay. *Sci. Rep.* **2021**, *11*, 13606. [CrossRef]
45. Revellame, E.D.; Fortela, D.L.; Sharp, W.; Hernandez, R.; Zappi, M.E. Adsorption kinetic modeling using pseudo-first order and pseudo-second order rate laws: A review. *Clean. Eng. Technol.* **2020**, *1*, 100032. [CrossRef]
46. Cameu, G.M.; Almeida, L.; Oliveira, A.P.; Igansi, A.; Jaeschke, D.P.; Silveira, N.; Paes, R.; Dias, D.; Pinto, L.A.d.A.; Cadaval, T.R.S. Enhanced Adsorption of Pb(II) and Cd(II) by Activated Carbon Derived from Peach Stones for Efficient Water Decontamination. *Processes* **2025**, *13*, 3064. [CrossRef]
47. Abdus-Salam, N.; Buhari, M. Adsorption of Alizarin and Fluorescein Dyes onto Palm Seeds Activated Carbon: Kinetic and Thermodynamic Studies. *J. Chem. Soc. Pak.* **2016**, *38*, 604–614.

48. Ncibi, M.C.; Sillanpää, M. Optimizing the removal of pharmaceutical drugs Carbamazepine and Dorzolamide from aqueous solutions using mesoporous activated carbons and multi-walled carbon nanotubes. *J. Mol. Liq.* **2017**, *238*, 379–388. [CrossRef]
49. Chibuzo, A.A.; Asadu, C.O.; Ikechukwu, O.M.; Arinze, A.K. Kinetics and isotherm studies on divalent lead ions adsorption by zeolite solution. *Int. J. Nov. Res. Eng. Sci.* **2016**, *3*, 49–61.
50. Elamin, M.R.; Abdulkhair, B.Y.; Elzupir, A.O. Removal of ciprofloxacin and indigo carmine from water by carbon nanotubes fabricated from a low-cost precursor: Solution parameters and recyclability. *Ain Shams Eng. J.* **2023**, *14*, 101844. [CrossRef]
51. Ibrahim, T.G.; Almufarij, R.S.; Abdulkhair, B.Y.; Ramadan, R.S.; Eltoum, M.S.; Elaziz, M.E.A. A Thorough Examination of the Solution Conditions and the Use of Carbon Nanoparticles Made from Commercial Mesquite Charcoal as a Successful Sorbent for Water Remediation. *Nanomaterials* **2023**, *13*, 1485. [CrossRef]
52. Adam, F.A.; Ghoniem, M.G.; Diawara, M.; Rahali, S.; Abdulkhair, B.Y.; Elamin, M.R.; Ben Aissa, M.A.; Seydou, M. Enhanced adsorptive removal of indigo carmine dye by bismuth oxide doped MgO based adsorbents from aqueous solution: Equilibrium, kinetic and computational studies. *RSC Adv.* **2022**, *12*, 24786–24803. [CrossRef] [PubMed]
53. Lima, E.C.; Hosseini-Bandegharaei, A.; Moreno-Piraján, J.C.; Anastopoulos, I. A critical review of the estimation of the thermodynamic parameters on adsorption equilibria. Wrong use of equilibrium constant in the Van't Hoof equation for calculation of thermodynamic parameters of adsorption. *J. Mol. Liq.* **2019**, *273*, 425–434. [CrossRef]
54. Vimonses, V.; Lei, S.; Jin, B.; Chow, C.W.; Saint, C. Kinetic study and equilibrium isotherm analysis of Congo Red adsorption by clay materials. *Chem. Eng. J.* **2009**, *148*, 354–364. [CrossRef]
55. Markeb, A.A.; Alonso, A.; Sánchez, A.; Font, X. Adsorption process of fluoride from drinking water with magnetic core-shell Ce-Ti@ Fe_3O_4 and Ce-Ti oxide nanoparticles. *Sci. Total Environ.* **2017**, *598*, 949–958. [CrossRef]
56. Ismail, B.; Hussain, S.T.; Akram, S. Adsorption of methylene blue onto spinel magnesium aluminate nanoparticles: Adsorption isotherms, kinetic and thermodynamic studies. *Chem. Eng. J.* **2013**, *219*, 395–402. [CrossRef]
57. Nguyen, T.H.T.; Dao, T.T.U.; Pham, G.V.; Do, T.S.; Nguyen, T.T.L.; Nguyen, T.H.L.; Chu, M.N.; Quoc, D.Q.N.; Tien, N.A. Effect of pH on the adsorption behaviour of Congo red dye on the Mg-Al layered double hydroxide. *IOP Conf. Ser. Mater. Sci. Eng.* **2020**, *736*, 022077. [CrossRef]

Disclaimer/Publisher's Note: The statements, opinions and data contained in all publications are solely those of the individual author(s) and contributor(s) and not of MDPI and/or the editor(s). MDPI and/or the editor(s) disclaim responsibility for any injury to people or property resulting from any ideas, methods, instructions or products referred to in the content.